DTU Library

Noise Phenomena in Electrochemical Impedance Spectroscopy of Polymer Electrolyte Membrane Electrolysis Cells

Elsøe, Katrine; Kraglund, Mikkel Rykær; Grahl-Madsen, L.; Scherer, G. G.; Hjelm, Johan; Jensen, Søren Højgaard; Jacobsen, Torben; Mogensen, Mogens Bjerg

Document Version
Publisher's PDF, also known as Version of record

Link back to DTU Orbit

Noise Phenomena in Electrochemical Impedance Spectroscopy of Polymer Electrolyte Membrane Electrolysis Cells▲

K. Elsøe[1]*, M. R. Kraglund[1], L. Grahl-Madsen[2], G. G. Scherer[3], J. Hjelm[1], S. H. Jensen[1], T. Jacobsen[4], M. B. Mogensen[1]

[1] Department of Energy Conversion and Storage, Technical University of Denmark, 4000 Roskilde, Denmark
[2] EWII Fuel Cells A/S, 5220 Odense SE, Denmark
[3] 5607 Hägglingen, Switzerland
[4] Department of Chemistry, Technical University of Denmark, Kemitorvet Building 207, DK-2800 Kgs. Lyngby, Denmark

Abstract

In this study, the origin of noise in electrochemical impedance spectroscopy (EIS) spectra measured on a variety of polymer electrolyte membrane electrolysis cells (PEMECs) has been investigated. EIS was measured during operation at various current densities of seven different PEMECs divided in five different cell types including both acidic PEMECs and alkaline PEMECs. The noise pattern differed between various types of cells and between cells of the same cell type. Integration time had no influence on the EIS noise level, whereas the AC amplitude seems to influence the EIS noise level. Other electrical noise sources influencing the EIS measurements have been studied with oscilloscope. No noise was observed at DC. A hypothesis explaining the relation between bubble formation during electrolysis and EIS noise is proposed based on the experimental findings.

Keywords: EIS, EIS Noise, Electrochemical Impedance Spectroscopy, Gas Bubbles, Nafion 117, PEMEC, Polymer Electrolyte Membrane Electrolysis Cell

1 Introduction

The amount of research within the area of water electrolysis has increased a lot during recent years, in particular research on PEMEC that presently is commercially available for demonstration purposes, but still far too expensive to compete with hydrogen production from fossil fuels. [1, 2] Therefore, improving the electrolysis cells and stacks is still needed, and for this we need to improve our methods for characterizing the electrolysis cells, in order to give proper feedback to the cell developers.

EIS is a strong and popular electrochemical characterization technique in electrochemical research in general and in the areas of fuel cell and battery research in particular. [3] How-ever, EIS has not been a preferred technique for investigation of PEMECs, and relatively few reports on systematic EIS studies can be found in literature. Among these studies some EIS data contains a limited amount of noise [4–6], whereas others do not contain any EIS noise [7–9]. The EIS noise phenomenon is to our knowledge never mentioned nor investigated. This article look into the EIS noise phenomenon, and experiments on both conventional acidic PEMECs and alkaline PEMECs with a KOH doped polybenzimidazole (PBI) membrane have been performed. We present a preliminary hypothesis on the mechanism of this noise as an AC perturbation interaction with gas bubbles adsorbed on the surface of the electrocatalyst.

[*] Corresponding author: katel@dtu.dk

▲ *Paper presented at the 6th EUROPEAN PEFC & ELECTROLYZER Forum (EFCF2017), July 4–7, 2017 held in Lucerne, Switzerland. Organized by the European Fuel Cells Forum – www.efcf.com*

2 Experimental

Various types of conventional acidic PEMECs and alkaline PEMECs have been studied with EIS during operation. All impedance data in this study has been analyzed using the impedance software Ravdav [10]. In this work, it has been chosen to report Bode plots showing the real part and the imaginary part of the EIS as functions of frequency, since these types of Bode plots very clearly show resistive and capacitive contributions to the total cell impedance, respectively, which is not the case for Bode plots depicting phase angle and modulus as functions of frequency.

2.1 Conventional Acidic Polymer Electrolyte Membrane Electrolysis Cells

Three types of PEMECs with Nafion 117 membranes produced by EWII Fuel Cells A/S (EWII) have been studied. All three cell types were of the same design with an active electrode area of 2.9 cm^2. Titanium felt was used as anode current collector, and the anode flow plate was interdigitated and made of titanium. The cathode catalyst loading was 0.5 mg cm^{-2} platinum (60 wt.% Pt/C), carbon felt was used as cathode current collector, and the cathode flow plate was made of carbon. Further information can be found elsewhere [11]. A schematic drawing of the cell and cell housing is shown in Figure 1. A more detailed schematic drawing of a benchmark PEMEC from EWII with scanning electron microscopy (SEM) images of the anode catalyst layer, the iridium metal current collector, the Ti-felt current collector and the carbon GDL can be seen in Figure 2.

The three conventional acidic PEMEC types studied differed in production generation and anode catalyst and were:
(i) A cell from an early generation production at EWII with 0.3 mg cm^{-2} IrO$_x$ as anode catalyst and a 1.7 mg cm^{-2} iridium metal contact layer (E-g1);
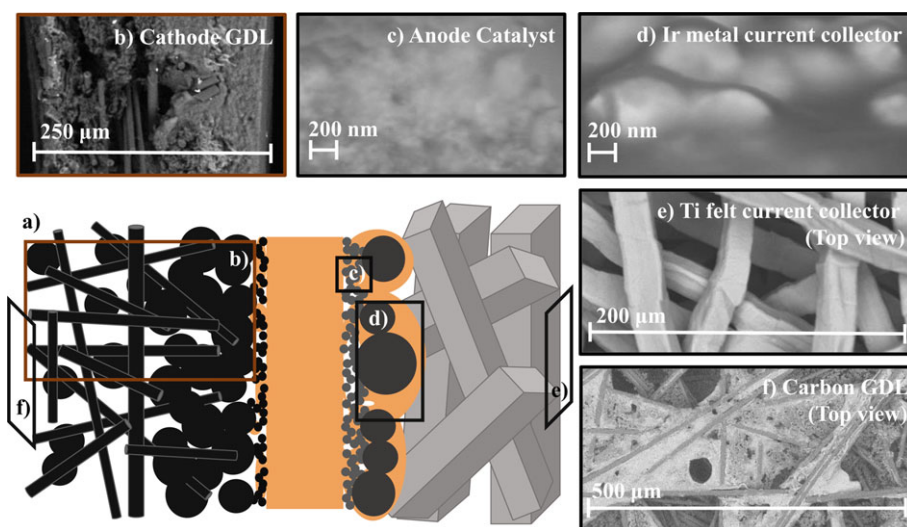

Fig. 2 Schematic drawing and SEM images of the microstructure of an EWII benchmark PEMEC (a). Image b, c and d are images of cross sections, whereas image e and f are images of the top of the anode Ti felt and the cathode carbon GDL, respectively.
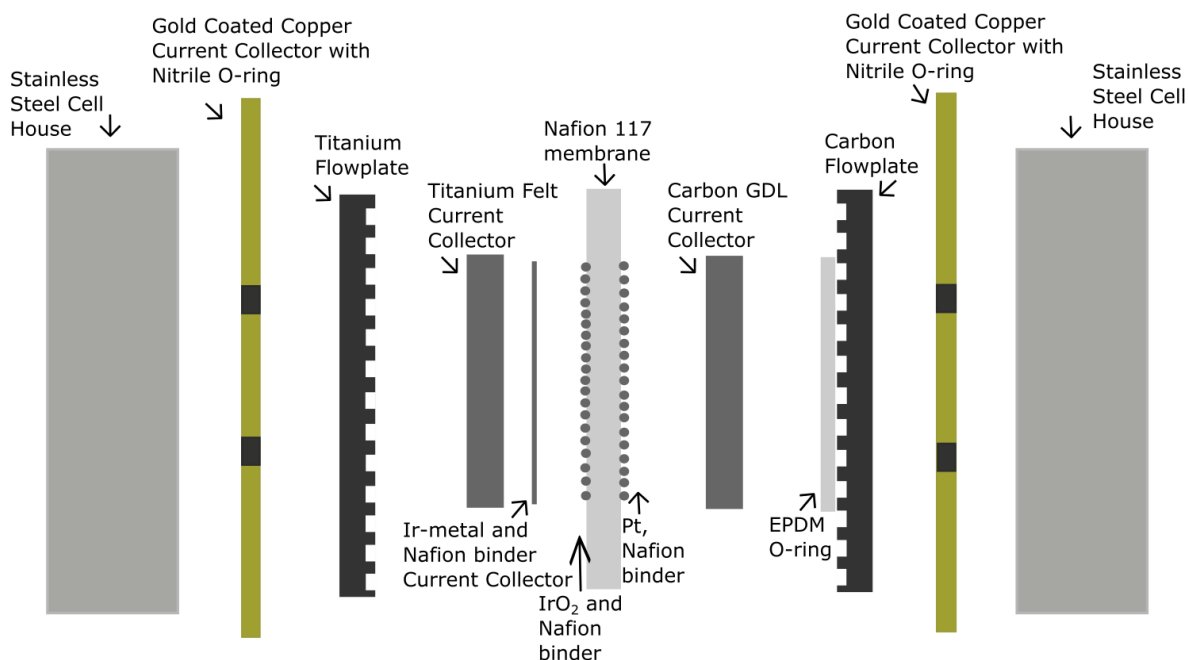

Fig. 1 Sketch of an expanded view of the PEMEC benchmark cell design of EWII cells [11].

(ii) A cell with 0.3 mg cm^{-2} anode catalyst consisting of 20 wt.% RuO$_2$ and 80 wt.% IrO$_x$ and a 2.5 mg cm^{-2} iridium metal contact layer (E-IrRu);

(iii) The more mature EWII benchmark PEMEC with 0.3 mg cm^{-2} IrO$_x$ as anode catalyst and a 2.7 mg cm^{-2} iridium metal contact layer. This is the cell that EWII uses as benchmark in the process of the further cell development. Three cells of the EWII benchmark type have been tested (E-ref-a, E-ref-b and E-ref-c).

2.1.1 Electrochemical Test Setup for Acidic PEMECs

All EIS measurements on conventional acidic PEMECs reported here were carried out at 61–65 °C. A Delta Elektronika ES 015-10 or a Delta Electronika SM 18-50 were applied for cell polarization. A 50 mΩ shunt resistance was serially connected to the cell for correct DC current determination. EIS was measured galvanostatically with a Solartron 1260 impedance analyzer, which was connected in parallel to the cell and shunt resistance. DC cancellation boxes were applied on the Solartron 1260 for improved AC signal resolution. 12 points were measured per frequency decade. The AC amplitude was 24.5–29.3 mA cm^{-2}, in most of the measurements, and in the few measurements, where other AC amplitudes have been applied on acidic PEMECs, it is given for the particular data in the corresponding text. The maximum frequency of EIS measured on acidic PEMECs shown in this article is 60 kHz, since above this frequency phase errors from the equipment, may influence the result. EIS measured at 45 and 54 Hz is left out of all the EIS plots, due to noise from the electrical grid. EIS measured on the EWII benchmark PEMEC named E-ref-a is only shown for frequencies above 0.10 Hz, due to an outlier in the measurements. The full EIS spectrum with outlier can be found in Figure A.1 in the Appendix. The anode of the acidic PEMECs were fed with Milli-DI water from Millipore at 300–500 mL min^{-1} during operation.

2.1.2 Oscilloscope Measurements

Electrochemical noise during DC operation of PEMECs was investigated, by measuring the cell potential of an operating benchmark PEMEC from EWII (E-ref-c) followed by fast Fourier transformation (FFT) of the signal with a digital differential oscilloscope from Picoscope. The oscilloscope was connected to the test setup *via* DC cancellation boxes, in order to increase the resolution of the noise signal. FFT of potential signals measured with the oscilloscope were generated by the oscilloscope software PicoScope6 using a Blackman filter. The measurements were done at a cell temperature of 64–66 °C and at two water flow rates.

2.2 Alkaline Polymer Electrolyte Membrane Electrolysis Cells

Two types of alkaline PEMECs have been studied with EIS and are schematically shown in Figure 3.

The two types were:

(i) A perforated nickel plate with a Raney-NiMo coating as cathode, a 40 µm m-PBI membrane and a perforated Ni plate as anode (R-NiMo│PBI│Ni), see Figure 3a (E-Ni-R).

(ii) A pressed Ni foam as cathode, a 40 µm m-PBI membrane and a perforated nickel plate as anode (Ni-foam│PBI│Ni) (E-Ni-F), see Figure 3b.

The used flow plates had a pin-type pattern and were made of Ni, PTFE was used as gasket material and the active electrode area was 25 cm^2.

Further details can be found elsewhere [12].

2.2.1 Electrochemical Test Setup for Alkaline PEMECs

The alkaline PEMECs were operated in partially separated mode in which 24 wt.% KOH (aq.) was circulated in independent electrolyte circuits. The anode flow was set to 50 mL min^{-1} for both alkaline PEMECs, whereas the cathode flow was depending on electrode geometry; 5 mL min^{-1} for the cathode of sample E-Ni-F, and 50 mL min^{-1} for the cathode of sample E-Ni-R. The electrolyte was flowed through a preheating cell prior to the electrolysis cell, to improve temperature stability at 80 °C. Heating was done by pairs of heating elements in the end-plates of both the pre-heating and the electrolysis cell.

EIS of the alkaline PEMECs was measured galvanostatically with a BioLogic Science Instruments HCP-1005 potentiostat in the frequency range 25 kHz – 0.1 Hz, however only EIS measured below 10 kHz is shown in this article due to outliers. EIS measured at 46 and 54 Hz is left out of all the EIS plots, due to noise from the electrical grid. The AC amplitude was 10% of the DC current applied to the cell and 15 points were measured per frequency decade.

3 Results and Discussion

3.1 EIS Noise Observed for Various PEMEC Types

The noise of the impedance spectra has been evaluated and quantified with a linear Kronig-Kramers transform compliance test, as reported by Boukamp [13]. The test gives an esti-
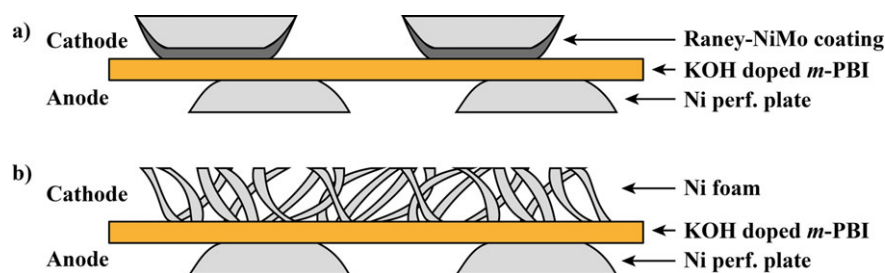

Fig. 3 Sketches of the two types of tested alkaline PEMECs.

Fuel Cells

mate on how well EIS data obey the four Kronig-Kramers relations; the system should show causality, be linear, stable and finite. In the linear Kronig-Kramers compliance test by Boukamp [13], measured EIS is fitted to multiple series connected Voigt elements (parallel R–C circuits) followed by calculating the relative Kramers-Kronig residuals as the difference between the fitted values and the measured impedance values at each frequency, according to Eq. (1)

$$\Delta_{re,i} = \frac{Z_{re,i} - Z_{re}(\omega_i)}{|Z(\omega_i)|} \quad and \quad \Delta_{im,i} = \frac{Z_{im,i} - Z_{im}(\omega_i)}{|Z(\omega_i)|} \tag{1}$$

with $Z_{re,i}$ and $Z_{im,i}$ being the real and imaginary parts of the ith data set impedance, and $Z_{re}(\omega_i)$ and $Z_{im}(\omega_i)$ being the fitted value of the real and the imaginary parts of the impedance for ω_i. $|Z(\omega_i)|$ is the absolute length of the modeling function [13]. Seven Voigt elements were applied per frequency decade for the calculations in this article. The Kramers-Kronig relative residuals can be used as a measure of the noise in the EIS spectra, as stochastic EIS noise would not obey the four Kramers-Kronig relations and therefore would increase the relative residuals in Boukamps Kramers-Kronig compliance test.

Figure 4 shows EIS measured on different PEMEC types shown in Bode plots and Kramers-Kronig relative residual plots, and EIS noise is observed in all the spectra. It should be noted that the operation current density is higher for the early generation EWII cell (E-g1) (1.00 A cm^{-2} compared to 0.35 or 0.40 A cm^{-2} for the other cells). However, since iV-curves of acidic PEMECs generally show a linear relation between current density and potential from current densities above approximately 0.35 A cm^{-2} [11], the differential cell resistance is constant for each PEMEC at current densities above 0.35 A cm^{-2}, and consequently the EIS of the various acidic PEMECs are comparable above this current density.

The noise of the EIS spectra have been further quantified, in order to be able to compare the overall noise level of the cells, by summing the squares of the relative residuals (both of the real and of the imaginary part of the impedance) over all measured frequencies, cf. Eq. (2), where δ is the overall noise level in %^{2}, $\Delta_{re,i}$ is the Kramers-Kronig relative residual of the real part of the impedance at frequency i in %, $\Delta_{im,i}$ is the Kramers-Kronig relative residual of the imaginary part of the impedance at frequency i in % and n is the maximum frequency measured.

$$\delta = \sum_{i=0}^{n} \Delta_{re,i}^2 + \Delta_{im,i}^2 \tag{2}$$

Table 1 compares the cell performance determined as the differential cell resistance, which is the real part of the impedance at very low frequency and the overall noise level, δ, of EIS depicted in Figure 4 measured on different cell types. No relation is observed between the cell performance and overall noise level of the cells, but EIS noise is observed for all six PEMECs. However, in this regard it should be noted that the frequency range over which δ has been determined varies a bit between the cells in Table 1. Figure A.2 in the Appendix compares EIS measured at 0.35 A cm^{-2} on three different cells of the same cell type (EWII benchmark cells; E-ref-a, E-ref-b and E-ref-c) and the cell performance and overall EIS noise level of these cells can be found in Table 1. From these table values, it can be seen that the overall EIS noise level varies between cells of the same cell type and not only between cells of different cell types.
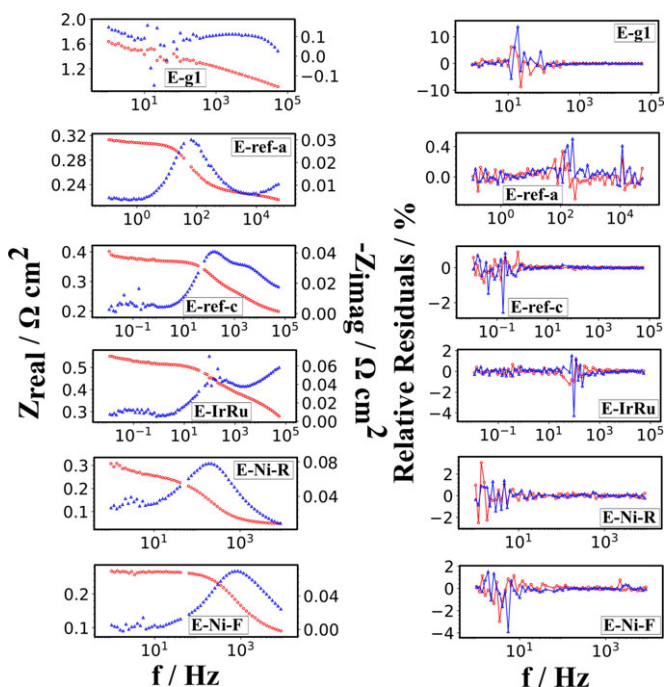

Fig. 4 EIS measured on six different PEMEC types: (E-g1) early generation acidic PEMEC from EWII at 0.35 A cm^{-2}, (E-ref-a) EWII benchmark PEMEC at 0.35 A cm^{-2}, (E-ref-c) another EWII benchmark PEMEC at 0.35 A cm^{-2}, (E-IrRu) EWII IrRuO$_x$ PEMEC at 0.35 A cm^{-2}, (E-Ni-R) Raney Ni alkaline PEMEC at 0.4 A cm^{-2} and (E-Ni-F) Ni foam alkaline PEMEC at 0.4 A cm^{-2}. Bode plots of the EIS data are shown in the left column and relative residuals of Kramers-Kronig compliance tests of the EIS data are shown in the right column. The real part of the impedance is shown with red circles, and the imaginary part of the impedance is shown with blue triangles.

Table 1 Operating current density, cell performance ($Z_{re,LF}$) and the overall EIS noise level, δ, for various PEMEC types.

Cell	Current Density / A cm^{-2}	$Z_{re,LF}$ / Ω cm^2	δ / %^{2}
E-g1	1.00	1.639	522.089
E-ref-a	0.35	0.316	1.664
E-ref-c	0.35	0.388	16.525
E-ref-b	0.35	0.367	258.341
E-IrRu	0.35	0.551	35.693
E-Ni-R	0.40	0.307	40.868
E-Ni-F	0.40	0.267	44.412

3.2 Influence of DC Load, AC Amplitude and Integration Time on EIS Noise

EIS measured at various DC current densities on four different acidic PEMECs (E-IrRu, E-ref-a, E-ref-b and E-ref-c) can be found in Figures A.3–A.6 in the Appendix, respectively. Tables 2–5 summaries the cell performances and the overall noise level given by the Kramers-Kronig residuals, δ, for the four cells at the various current densities. Based on the four tables, no clear relation is observed between operating DC current density and the overall EIS noise level.

EIS measured at various AC amplitudes on two EWII benchmark PEMECs (E-ref-b and E-ref-c) can be found in Figures A.7 and A.8 in the Appendix, respectively. Tables 6 and 7 summaries the overall noise, δ, for the two cells at various AC amplitudes. The results indicate increasing overall EIS noise with decreasing AC amplitude.

Figure A.9 shows the influence of integration time applied when measuring EIS on the noise level of the EIS spectra measured at 0.35 A cm^{-2} on an EWII benchmark cell (E-ref-c). The

Table 2 Cell performance ($Z_{re,LF}$) and the overall EIS noise level, δ, for the IrRuO$_x$ PEMEC from EWII (E-IrRu) measured at various current densities.

Current Density / A cm^{-2}	$Z_{re,LF}$ / Ω cm^2	δ / %^{2}
0.07	0.922	1.872
0.35	0.549	35.693
0.69	0.450	8.988
1.00	0.439	15.857

Table 3 Cell performance ($Z_{re,LF}$) and the overall EIS noise level, δ, for the EWII benchmark cell, E-ref-a, measured at various current densities.

Current Density / A cm^{-2}	$Z_{re,LF}$ / Ω cm^2	δ / %^{2}
0.07	0.531	1.619
0.35	0.316	1.664
0.69	0.311	5.434
1.00	0.311	2.829

Table 4 Cell performance ($Z_{re,LF}$) and the overall EIS noise level, δ, for the EWII benchmark cell, E-ref-b, measured at various current densities.

Current Density / A cm^{-2}	$Z_{re,LF}$ / Ω cm^2	δ / %^{2}
0.07	0.574	196.913
0.35	0.324	258.341
0.69	0.298	180.162
1.00	0.276	267.354
2.00	0.248	176.164

Table 5 Cell performance ($Z_{re,LF}$) and the overall EIS noise level, δ, for the EWII benchmark cell, E-ref-c, measured at various current densities.

Current Density / A cm^{-2}	$Z_{re,LF}$ / Ω cm^2	δ / %^{2}
0.35	0.313	16.525
1.00	0.402	14.779

Table 6 Overall EIS noise level, δ, for the EWII benchmark cell, E-ref-b, measured at various AC amplitudes and at 0.35 A cm^{-2}.

Amplitude / mA cm^{-2}	δ / %^{2}
29.3	298.919
14.6	660.659
4.9	5525.466

Table 7 Overall EIS noise level, δ, for the EWII benchmark cell, E-ref-c, measured at various AC amplitudes and at 0.35 A cm^{-2}.

Amplitude / mA cm^{-2}	δ / %^{2}
29.3	16.525
14.6	239.378

integration time denotes the period over which the EIS analyzer is measuring the perturbation signal [14]. This means that white stochastic noise will be cancelled out the more the longer the integration time is. Table 8 lists the overall noise level at the various integration times.

Based on Table 8, the EIS noise level is not influenced by integration time.

3.3 Investigations of Noise Sources with Oscilloscope

Sources of electrical noise have been investigated with oscilloscope by measuring the potential across an EWII benchmark PEMEC (E-ref-c) operated at 1.00 A cm^{-2} and with various water flow speed. Figure 5 shows the fast Fourier transform (FFT) of the potential measured across the PEMEC at various water flow speeds. Graph a in Figure 5 is measured at a high water flow speed, whereas graph b in Figure 5 is measured at a lower water flow. Clear changes in the magnitude and frequency of the noise peaks with changes in water flow speed is observed; the lower the water flow the lower the noise magnitude and the lower the frequency of the noise. At high water flow speed noise is observed slightly above 50 Hz, 100 Hz, 150 Hz, and 200 Hz, whereas at low water flow speed noise is observed at lower frequencies at approximately 20 Hz, 40 Hz, 60 Hz, and 80 Hz. These findings imply that the water pumps introduce electrical noise in the PEMEC system. However, the noise peak at 167 Hz does not change with the water flow speed.

It was speculated whether the noise introduced by the water pumps was caused by pressure changes in the gas

Table 8 Overall EIS noise level, δ, for the EWII benchmark cell, E-ref-b, measured at various integration times and at 0.35 A cm^{-2} and with an AC amplitude of 29.3 mA cm^{-2}.

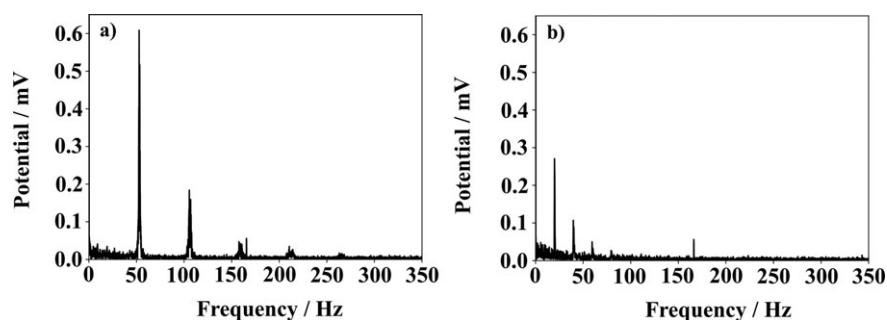| Integration Cycles	δ / %^{2}
96	298.919
40	259.869
5	278.756
1	236.226

Fig. 5 FFT of potential measured with an oscilloscope across an EWII benchmark PEMEC (E-ref-c) during operation at 1.00 A cm^{-2} at with the pumps operating at high water flow speed (a) and with the pumps operating at low water flow speed (b). The two graphs show only the frequency range 0–350 Hz, since no peaks were observed above 350 Hz.

evolved at the electrodes in the PEMEC causing changes in the cell potential as function of the water flow changes, or whether the noise was introduced as electrical disturbances from the motor of the water pump. A cable applied as antenna able to record possible electrical interferences from the motor was held in the open air close to the water pump, and noise was recorded as can be seen in Figure 6. Graph b in Figure 6 is measured with the cable while operating the water pump at low water flow speed, and noise is observed at approximately 20 Hz, 40 Hz, 60 Hz, and 80 Hz. These frequencies correspond to the frequencies at which noise was observed in Figure 5 b for the PEMEC operated with at low water flow rate. This imply that the electrical noise observed during DC operation of the PEMEC is due to electrical disturbances from the motor of the water pump and not due to pressure changes in the PEMEC due to the water flowrate. Furthermore, the graphs in Figure 6 show potential peaks at 50 Hz, 100 Hz, and 150 Hz, which is expected to originate from electrical interferences from the 220 V electrical grid in the lab building.

3.4 EIS Noise Originating from Gas Bubbles – A Hypothesis

Our hypothesis explaining the noise observed in the EIS spectra recorded on various types of PEMECs is that the noise originates from gas bubbles partially covering the electrodes of the PEMECs during operation. The noise in the EIS spectra

occurs at various frequencies depending on the particular cell, and not only at the frequencies, where noise from the water pumps was observed, according to the oscilloscope measurements reported in Figures 5 and 6. Therefore, it can be concluded that the EIS noise is not caused by electrical noise from the water pumps or any electrical noise from other sources than the cells. Since the noise is observed in many different PEMECs, it is expected that the EIS noise is caused by a physical process associated with the operation of a PEMEC. Another indication that the EIS noise is caused by a physical process is that the noise seems independent of integration time, cf. Table 8 and Figure A.9. If white electrical noise caused the EIS noise, an increase in integration time would decrease the noise level.

One may think that the suggested hypothesis imply the gas bubbles to be formed and released at a particular frequency depending on the DC magnitude and the microstructure of the cell. However, the FFT potential measurements in Figure 5, recorded during DC operation of a PEMEC with no AC perturbation, show only noise signals associated with the motor of the water pump. The lack of electrical noise from the cell during DC operation can be explained by a completely stochastic release of the gas bubbles across the electrode surface. During DC operation, the bubble coverage of the PEMEC electrodes will be in a quasi-steady-state where the average release rate of bubbles from the total electrode surface will be constant. When applying an AC potential on top of the DC operation potential, the bubble coverage of the PEMEC electrodes will no longer be in a quasi-steady-state, but will fluctuate with the AC signal leading to a non-constant (unstable) average release rate of the bubbles from the total electrode surface. The AC perturbation applied to the cell during EIS measurements may synchronize the release of bubbles across the electrode surface, causing the bubble release rate to preferably take place in an unstable manner at particular resonance frequency ranges for some bubble sizes dependent on the microstructure of the particular PEMEC. This will cause EIS noise in a narrow frequency range in the EIS spectrum dependent on the particular PEMEC. A schematic drawing and SEM images of the microstructure of a conventional acidic PEMEC from EWII is seen in Figure 2. Gas bubbles may be trapped in various locations on the active electrode in the microstructure such as in the anode catalyst layer blocking the current path and thereby locally increasing the potential, which is leading to EIS noise. These trapped bubbles will vibrate when the AC current is applied, due to fluctuations in the gas formation rate with the AC signal, and thereby the bubbles will be
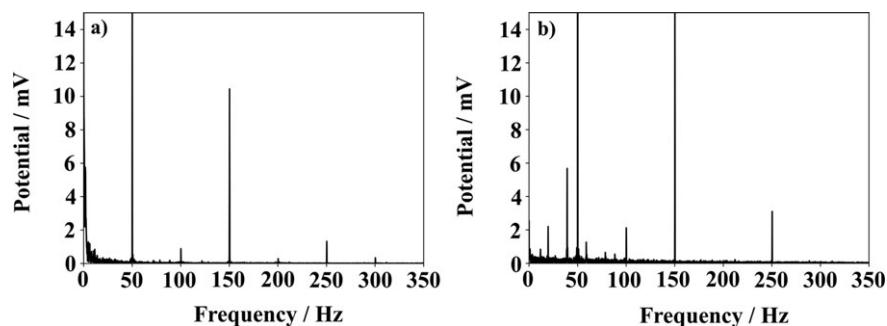

Fig. 6 FFT of potential measured on a cable applied as antenna in air close to the water pump supplying water to an operating EWII benchmark cell (cell 5) at high water flow speed (a) and at low water flow speed (b). The two graphs show only the frequency range 0–350 Hz, since no peaks were observed above 350 Hz.

released at certain frequencies. The optimal microstructure should have a sufficiently open structure, which enables gas bubble release from the electrocatalyst while the bubbles are small, leading to low or no noise in the EIS spectra. In this regard it shall be noted that the EIS noise reported in literature is not in conflict with this hypothesis [4–9].

4 Conclusions

A number of different PEMECs were investigated by EIS with respect to their noise pattern.

EIS noise from the electrodes was observed in one narrow frequency range for a number of different PEMECs. The EIS noise was found to be independent on cell internal resistance and EIS integration time. The EIS noise seems to increase with decreasing AC amplitude. A hypothesis has been presented, which suggests a constant bubble release rate from the electrocatalyst during DC operation leading to no electrochemical noise and a non-constant bubble release rate when an AC is overlaid the DC leading to electrical noise at resonance frequencies dependent on the particular microstructure of the PEMEC.

Acknowledgements

Appendix

Figure A.1 shows the full EIS spectrum with outlier measured at 0.35 A cm^{-2} on the EWII benchmark cell, E-ref-a. EIS spectra measured on the same cell at other current densities showed identical outliers. Figure A.2 compares EIS measured at 0.35 A cm^{-2} on three different cells of the same cell type (EWII benchmark cells; E-ref-a, E-ref-b and E-ref-c).

EIS measured at various DC current densities on four different acidic PEMECs (E-IrRu, E-ref-a, E-ref-b and E-ref-c) are shown in Figures A.3–A.6, respectively. EIS measured at various AC amplitudes on two EWII benchmark PEMECs (E-ref-b and E-ref-c) can be found in Figures A.7 and A.8, respectively, and Figure A.9 shows the influence of integration time on the overall noise level of the EIS spectra measured at 0.35 A cm^{-2} on an EWII benchmark cell (E-ref-c).
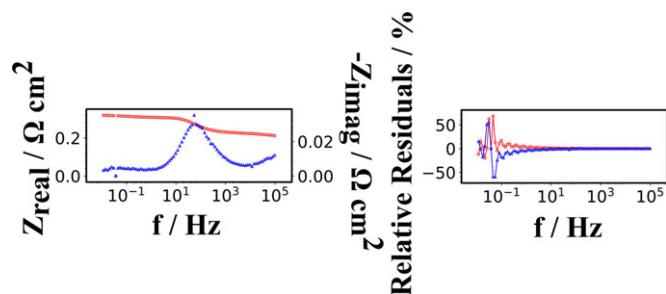

Fig. A.1 EIS spectrum measured at 0.35 A cm^{-2} on an EWII benchmark cell (E-ref-a). The full frequency range is shown with outliers. Bode plots of the EIS data are shown in the left column and relative residuals of Kramers-Kronig compliance tests of the EIS data are shown in the right column. The real part of the impedance is shown with red circles, and the imaginary part of the impedance is shown with blue triangles.
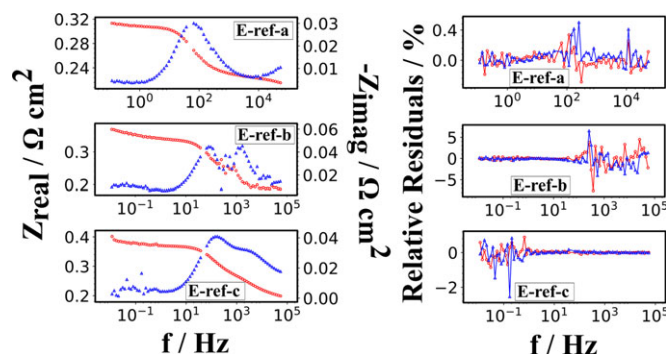

Fig. A.2 EIS measured on three different cells of the same EWII benchmark cell type at 0.35 A cm^{-2}: E-ref-a, E-ref-b, E-ref-c. An AC amplitude of 24.5 mA cm^{-2} was applied on E-ref-a, and an AC amplitude of 29.3 mA cm^{-2} was applied when measuring on E-ref-b and E-ref-c. Bode plots of the EIS data are shown in the left column and relative residuals of Kramers-Kronig compliance tests of the EIS data are shown in the right column. The real part of the impedance is shown with red circles, and the imaginary part of the impedance is shown with blue triangles.
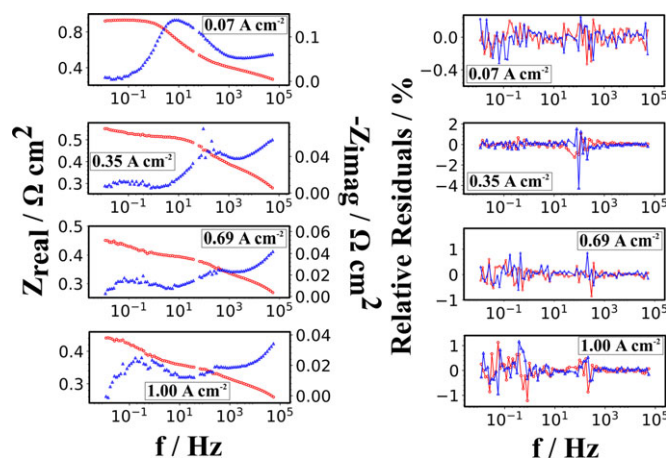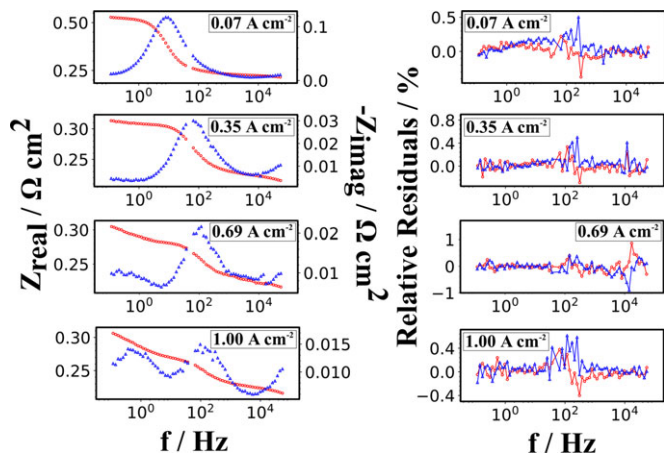

Fig. A.3 EIS measured at four different current densities (0.07, 0.35, 0.69, and 1.00 A cm^{-2}) on the IrRuOx PEMEC from EWII (E-IrRu). The AC amplitude was 24.5 mA cm^{-2}. Bode plots of the EIS data are shown in the left column and relative residuals of Kramers-Kronig compliance tests of the EIS data are shown in the right column. The real part of the impedance is shown with red circles, and the imaginary part of the impedance is shown with blue triangles.

Fig. A.4 EIS measured at four different current densities (0.07, 0.35, 0.69, and 1.00 A cm^{-2}) on the EWII benchmark cell, E-ref-a. The AC amplitude was 24.5 mA cm^{-2}. Bode plots of the EIS data are shown in the left column and relative residuals of Kramers-Kronig compliance tests of the EIS data are shown in the right column. The real part of the impedance is shown with red circles, and the imaginary part of the impedance is shown with blue triangles.
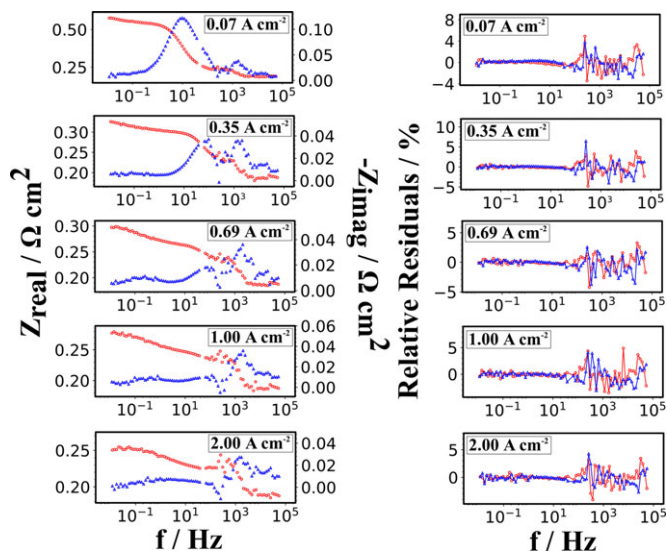

Fig. A.6 EIS measured at two different current densities (0.35 and 1.00 A cm^{-2}) on the EWII benchmark cell, E-ref-c. The AC amplitude was 29.3 mA cm^{-2}. Bode plots of the EIS data are shown in the left column and relative residuals of Kramers-Kronig compliance tests of the EIS data are shown in the right column. The real part of the impedance is shown with red circles, and the imaginary part of the impedance is shown with blue triangles.
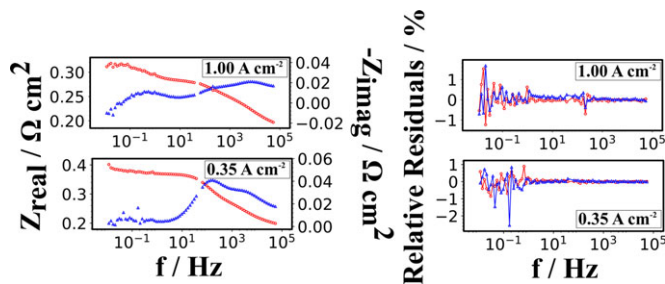

Fig. A.5 EIS measured at five different current densities (0.07, 0.35, 0.69, 1.00, and 2.00 A cm^{-2}) on the EWII benchmark cell, E-ref-b. The AC amplitude was 29.3 mA cm^{-2}. Bode plots of the EIS data are shown in the left column and relative residuals of Kramers-Kronig compliance tests of the EIS data are shown in the right column. The real part of the impedance is shown with red circles, and the imaginary part of the impedance is shown with blue triangles.
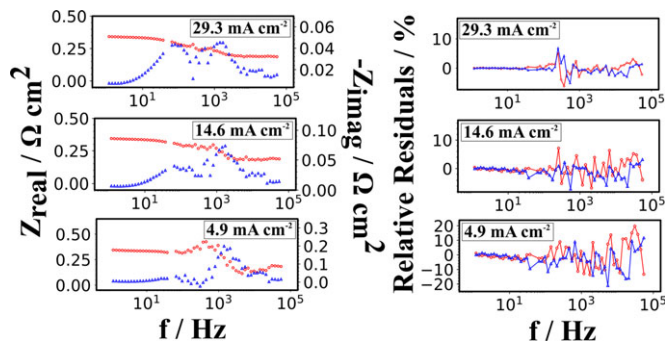

Fig. A.7 EIS measured at three different AC amplitudes (29.3, 14.6, and 4.9 mA cm^{-2}) on the EWII benchmark cell, E-ref-b, at 0.35 A cm^{-2}. Bode plots of the EIS data are shown in the left column and relative residuals of Kramers-Kronig compliance tests of the EIS data are shown in the right column. The real part of the impedance is shown with red circles, and the imaginary part of the impedance is shown with blue triangles.
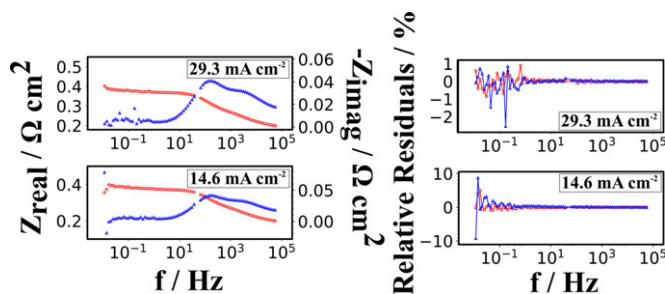

Fig. A.8 EIS measured at two different AC amplitudes (29.3 and 14.6 mA cm^{-2}) on the EWII benchmark cell, E-ref-c, at 0.35 A cm^{-2}. Bode plots of the EIS data are shown in the left column and relative residuals of Kramers-Kronig compliance tests of the EIS data are shown in the right column. The real part of the impedance is shown with red circles, and the imaginary part of the impedance is shown with blue triangles.

Fig. A.9 EIS measured at four different integration times (96, 40, 5, and 1) on the EWII benchmark cell, E-ref-b, at 0.35 A cm^{-2}. Bode plots of the EIS data are shown in the left column and relative residuals of Kramers-Kronig compliance tests of the EIS data are shown in the right column. The real part of the impedance is shown with red circles, and the imaginary part of the impedance is shown with blue triangles.
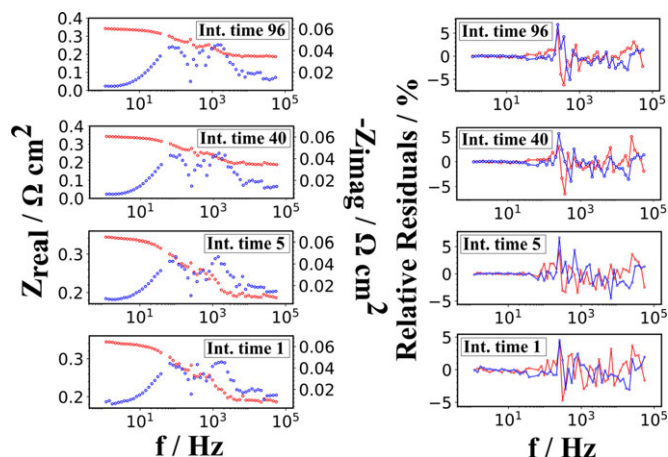
References

[1] M. Carmo, D. L. Fritz, J. Mergel, D. Stolten, *Int. J. Hydrogen Energy* **2013**, *38*, 4901.

[2] U. Babic, M. Suermann, F. N. Büchi, L. Gubler, T. J. Schmidt, *J. Electrochem. Soc.* **2017**, *164*, F387.

[3] E. Barsoukov, J. R. Macdonald, *Impedance Spectroscopy – Theory, Experiment, and Applications*, Second edition, John Wiley & Sons, Hoboken, New Jersey, **2005**.

[4] I. Dedigama, P. Angeli, K. Ayers, J. B. Robinson, P. R. Shearing, D. Tsaoulidis, D. J. L. Brett, *Int. J. Hydrogen Energy* **2014**, *39*, 4468.

[5] C. Rakousky, U. Reimer, K. Wippermann, M. Carmo, W. Lueke, D. Stolten, *J. Power Sources* **2016**, *326*, 120.

[6] C. Rozain, P. Millet, *Electrochim. Acta* **2014**, *131*, 160.

[7] S. Siracusano, V. Baglio, F. Lufrano, P. Staiti, A. S. Aricò, *J. Membr. Sci.* **2013**, *448*, 209.

[8] P. Lettenmeier, S. Kolb, F. Burggraf, A. S. Gago, K. A. Friedrich, *J. Power Sources* **2016**, *311*, 153.

[9] P. Lettenmeier, R. Wang, R. Abouatallah, S. Helmly, T. Morawietz, R. Hiesgen, S. Kolb, F. Burggraf, J. Kallo, A. S. Gago, K. A. Friedrich, *Electrochim. Acta* **2016**, *210*, 502.

[10] C. Graves, Ravdav data analysis software, version 0.9.7, **2012**.

[11] K. Elsøe, L. Grahl-Madsen, G. G. Scherer, J. Hjelm, M. B. Mogensen, *J. Electrochem. Soc.* **2017**, *164*, F1419.

[12] M. R. Kraglund, *PhD thesis*, DTU Energy, **2017**.

[13] B. A. Boukamp, *J. Electrochem. Soc.* **1995**, *142*, 1885.

[14] Solartron Analytical, 1260 Impedance/Gain-Phase Analyzer – Operating Manual, **1996**.